Kinematic and Dynamic Modelling of a Snake-Arm Manipulator Section for In-plane Motion ⋆

Gustavo C. Rodrigues * **Rafael A. C. Laranja** * **Walter F. Lages** **
Mário R. S. Sobrinho * **Eduardo A. Perondi** *

* *Departamento de Engenharia Mecânica, Universidade Federal do Rio Grande do Sul, Porto Alegre.*
{gustavo.comerlato, rafael.laranja, mario.sobczyk, eduardo.perondi}@ufrgs.br.
** *Departamento de Sistemas Elétricos de Automação e Energia, Universidade Federal do Rio Grande do Sul, Porto Alegre.*
fetter@ece.ufrgs.br

Abstract: Herein we develop and discuss two models for tendon-driven continuum robots comprising multiple sections. The first model is a simple constant-curvature one, commonly used in inverse-kinematics and trajectory-planning tasks for small and light continuum robots; the second is a rigid-body dynamic one, useful for simulations and studying control strategies. The models are compared to data from a simple prototype pseudocontinuum manipulator for pipeline inspections. Results show that the rigid body model represents more adequately the operation of the prototype in both static and dynamic tests.

Keywords: Continuum Robotics, Underactuated Systems, Field Robotics, Systems Modelling.

1. INTRODUCTION

Robotics as a field has broadened its scope considerably since its first industrial applications in the first half of the 20$^{\text{th}}$ century (Siciliano and Khatib, 2016). In the early 21$^{\text{st}}$ century it has become commonplace to find robotic systems in applications such as search and rescue in man-made or natural environments, inside pipelines and jet engines, or even the human body itself (Dupont et al., 2022). Given this extension in their application domains, it is no surprise that the shape of robots themselves has also changed. This is the case of so-called "soft robots", which are robotic systems which are passively compliant, and possess several (ideally infinite) degrees of freedom to facilitate interactions with their working environment (Russo et al., 2023).

As shown in Russo et al. (2023) many recent works have discussed continuum and soft robotic designs. One of the most well-known of such architectures is a class of slender, hyper-redundant robots referred to as "Continuum Robots", which are especially suited for confined environments. This class includes the so-called "rigid backbone" robots, which may be constructed with rolling contact joints (Suh et al., 2015), hybrid mechanisms with both "soft" and "hard" sections, or even structures with no flexible parts at all (Ay, 2023). Such robots have been modeled in a number of ways, with *Constant-Curvature Kinematic* (CCK) models appearing as one of the simples and most popular model classes. Those models provide a direct approximation of the robot's bending motion as that of a circular arc, as discussed in Webster and Jones (2010) and Allen et al. (2020). This approach is adequate in the absence of external forces (such as gravity) or friction phenomena, and if the robot is uniformly stiff along its length. Such models are also common in path-planning and inverse kinematics tasks, as they can be used to derive analytical expressions and are simple enough for real-time execution.

A second widely used class of models is that of Cosserat rods (Boyer et al., 2021; Gazzola et al., 2018), which approximate continuum robots as the limit case of a hyperredundant manipulator with infinitely many rigid links, separated by infinitesimal motions. These rods are Reissner beam models (Boyer et al., 2021) with extensional, bending, shearing, and torsional deformation modes, but differ from, traditional beam models in that they are *geometrically exact*, typically based on space curves equipped with Bishop's frames and kinematic reconstruction equations. This approach's key advantage is the direct connection with discrete robot kinematics and dynamics (Boyer et al., 2021), which allows one to almost directly adapt tools and results from robotic manipulators to continuum robots, as well as high levels of shape accuracy and being amenable to real-time simulation.

In this work, we consider the modelling of a prototype continuum robot, comprising a series of disks interconnected by spherical joints and helicoidal springs, including dry friction effects in both joint and cable dynamics. Parallel cables passing through the disks are used to actuate the system by increasing or reducing their traction forces. This

⋆ This work has been partially funded by the Brazilian agency CAPES.

configuration is called a "snake-arm" robot, illustrated in Figure 1.

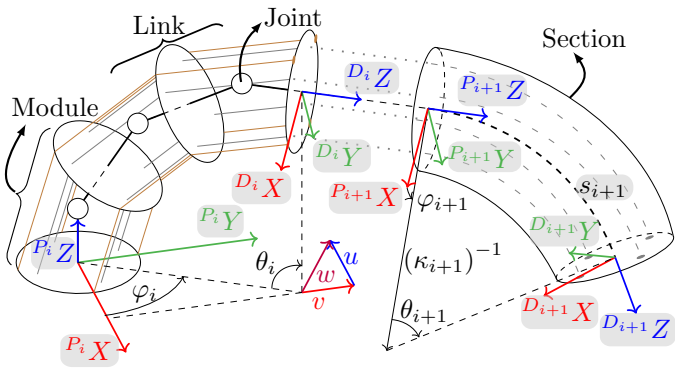

Figure 1. Snake-arm robot with its descriptive convention.

This paper is structured as follows: In Section 2, we describe the two kinematic and dynamic models analyzed here, with the corresponding procedures for their numerical implementation. Section 3 describes the Annelida prototype robot's main features. In Section 4, we evaluate the ability of both models to reproduce the Annelida robot's experimental behavior. Finally, in Section 5 we summarize and discuss this paper's findings.

2. SYSTEM MODELLING

A typical "snake-arm" robot is actuated by fluidic systems or, as in the present case, by taut strings emulating animal tendons. A tendon-driven continuum robots is comprised of several *modules*, often grouped in *sections*. Figure 2 depicts one such module. It comprises two links connected by a spherical joint actuated by four tendons, regarded as a closed kinematic chain with prismatic joints for the cables in the system's kinematic analysis.

Figure 2 shows a module of a snake-arm robot with a spherical joint with taut cables, regarded as a closed kinematic chain with linear joints for the cables for the kinematic analysis.

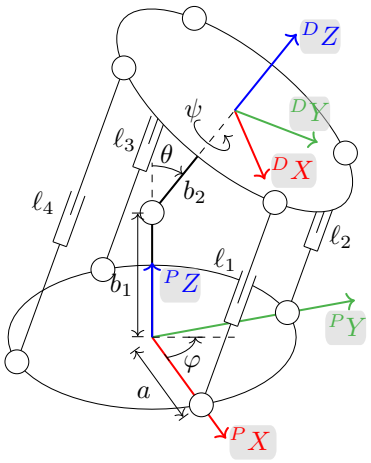

Figure 2. Module of a Snake-arm robot as a closed kinematic chain.

2.1 Kinematic analysis

The kinematic analysis of traditional robots is based on their *joint* and *task* spaces, $\mathcal{Q} = \{\mathbf{q} \in \mathbb{R}^{n_j} | \underline{q}_i \leq q_i \leq \overline{q}_i, i = 1 \dots n_j\}$ and $\mathcal{X} = \{{}^0\mathbf{X}_i | {}^0\mathbf{X}_i \in SE(3), i = 1 \dots n_l\}$ respectively, where n_j and n_l are the corresponding numbers of joint and link position coordinates. For continuum robots, a third coordinate space is added, the *configuration space* $\mathcal{Z}$. This intermediate mapping can be understood as a sort of "modal decomposition", explained in detail in Chirikjian and Burdick (1994) by relating the individual joint values to the overall robot pose in $\mathcal{X}$ via a combination of shape functions, which depend upon the particular modelling framework chosen. In the case of CCK models, for instance, the shape functions form circular arcs parameterized by three parameters per continuum section, which correspond to the first bending and extensional modes of deformation with constant strain along the beam.

Usually, there are two main parametrizations for constant-curvature models. The first is the so-called "Jones" parameterization (Webster and Jones, 2010; Frazelle, 2021), where the space curve of a section is a function of its azimuth ϕ, curvature κ and arc length s, akin to an Euler angle approach. The second parameterization is the "Allen" parameterization (Allen et al., 2020; Frazelle, 2021), which is based on screw theory and bypasses the singularity at the straight rod configuration. Its parameters are $w = (u, v, 0)$, the twist vector, and s. Both parameterizations can be converted between each other by the following:

$$\begin{aligned} \theta = s\kappa = \|w\| = \sqrt{(u^2 + v^2)} \\ \varphi = \arctan 2(-u, v) \\ (u, v) = (-\theta \sin\varphi, \theta \cos\phi) \end{aligned} \tag{1}$$

Thus, by the Allen parameterization, one can write the transformation matrix ${}^{P_i}T_{D_i}$ which relates the distal frame D_i of a section to its proximal frame P_i, with $\xi := \operatorname{sinc} \|w\|$ and $\gamma := \frac{1}{2} \operatorname{sinc}^2 \frac{\|w\|}{2}$. This is the forward kinematics map from configuration space to task space:

$${}^{P_i}T_{D_i} = \begin{bmatrix} \xi_i v_i^2 + 1 & -\gamma_i u_i v_i & \xi_i v_i & -s_i v_i \gamma_i \\ -\gamma_i u_i^2 v_i & \gamma_i u_i^2 + 1 & -\xi_i u_i & s_i u_i \gamma_i \\ -\xi_i v_i & \xi_i u_i & \cos\|w\| & \xi_i s \\ 0 & 0 & 0 & 1 \end{bmatrix} \tag{2}$$

The inverse kinematics of the section are given by:

$$\begin{aligned} \varphi_i &= \operatorname{atan2}\left({}^{P_i}y, {}^{P_i}x\right) \\ \kappa_i &= \frac{2}{\|\mathbf{x}\| \sqrt{{}^{P_i}x^2 + {}^{P_i}y^2}} \\ \theta_i &= \operatorname{acos}\left(1 - \kappa_i \sqrt{{}^{P_i}x^2 + {}^{P_i}y^2}\right) \end{aligned} \tag{3}$$

The inverse kinematics of a module give the tendon lengths as a function of its joint angles, which are obtained directly by:

$$\ell_i = \left\| {}^{P_i}T_{D_i}\mathbf{c}_j - \mathbf{c}_j \right\| \tag{4}$$

The forward kinematics of the module, for the case of zero torsion, $\psi = 0$, are similarly given by:

$$\begin{aligned} \varphi_i &= \operatorname{atan2}\left({}^i\ell_4 - {}^i\ell_2, {}^i\ell_3 - {}^i\ell_1\right) \\ \kappa_i &= \frac{\left({}^i\ell_1 - 3{}^i\ell_2 + {}^i\ell_3^i\ell_4\right)\sqrt{\left({}^i\ell_4 - {}^i\ell_2\right)^2 + \left({}^i\ell_3 - {}^i\ell_1\right)^2}}{a_i\left({}^i\ell_1 + {}^i\ell_2 + {}^i\ell_3^i\ell_4\right)\left({}^i\ell_4 - {}^i\ell_2\right)} \\ \theta_i &= \frac{2n_{j,i}}{\kappa_i} \operatorname{atan2}(\kappa_i b_i) \end{aligned} \tag{5}$$

One should note however that the forward kinematics map is only well-defined when there are at most four tendons for a snake-arm module, as a consequence of the Carathéodory theorem (Murray et al., 1994).

2.2 Dynamic modelling

The dynamic model of the snake-arm robot can be obtained in Euler-Lagrangian form, as detailed in standard robotics textbooks (Murray et al., 1994; Featherstone, 2008; Lynch and Park, 2017), giving rise to the following joint space dynamics:

$$\mathbf{M}\ddot{\theta} + \mathbf{C}\dot{\theta} + \mathbf{G} + \mathbf{K}\theta + \mathbf{F} = \mathbf{J}_S^T \mathbf{W}\mathbf{B}\mathbf{u} \tag{6}$$

where θ are the joint coordinates, $\mathbf{M}$ and $\mathbf{C}$ are the generalized joint-space inertia and Coriolis/centrifugal force matrices, $\mathbf{G}$ is the vector of joint forces due to gravity, $\mathbf{K}$ is a diagonal joint stiffness matrix, and $\mathbf{F}$ contains joint friction forces. On the right side, $\mathbf{J}_S^T$ is the transposed system Jacobian, $\mathbf{W}$ is a matrix which transforms tendon tensions to equivalent link wrenches, and $\mathbf{B}$ maps tendon tensions at the base to tensions at each module. The exact expressions for matrices $\mathbf{M}$, $\mathbf{C}$, $\mathbf{G}$ can be obtained analytically via screw-theoretical formulas, as exposed in works such as (Murray et al., 1994; Lynch and Park, 2017; Mueller, 2018).

To include friction effects in this model, we use the vector $\mathbf{F}$ which contains joint friction forces. Here we use a static friction model which accounts for both dry and viscous friction, as well as the Stribeck effect. The discontinuity at the origin is smoothed by the hyperbolic tangent function using a high enough value of k_v, in order to make the simulation amenable for numerical solvers. The friction torques equivalent for each joint are then given by the following equation:

$$\mathbf{F}_i = \tau_\mu \dot{\theta}_i + \tau_c \tanh\left(k_v \dot{\theta}_i\right)\left(1 + S\exp^{-\left(\dot{\theta}_i/v_d\right)^2}\right) \tag{7}$$

where τ_c is the Coulomb dry friction torque magnitude, τ_μ is the viscous friction coefficient, S is the relative size of the Stribeck effect and v_d is the Stribeck speed. On the right side of (6), $\mathbf{B}$ propagates applied tendon tensions $\mathbf{u}$ at the base to tensions at each module via the Capstan friction relation:

$$\mathbf{B} = \begin{bmatrix} \mathbf{I}\exp\left(-\mu_c \frac{\theta_1}{2}\right) \\ \mathbf{I}\exp\left(-\mu_c\left(\theta_1 + \frac{\theta_2}{2}\right)\right) \\ \vdots \\ \mathbf{I}\exp\left(-\mu_c\left(\theta_1 + \cdots + \frac{\theta_{n_j}}{2}\right)\right) \end{bmatrix} \tag{8}$$

The matrix $\mathbf{W}$ in Eq. (6) relates tendon tensions at each module resulting from the Capstan relation to equivalent external wrenches applied at the center of mass (CoM) of each link, in body coordinates. Figure 3 illustrates this relation for the bidimensional case.

Finally, $\mathbf{J}_S^T$ is the system transposed jacobian matrix, which transforms wrenches in body coordinates to equivalent joint torques. It has the following upper block triangular structure, in the same vein of the expressions given in Renda et al. (2018) and Mueller (2018), where each block jacobian ${}^i\mathbf{J}_j^T$ converts wrenches in body j's CoM to body i's joint coordinate system:

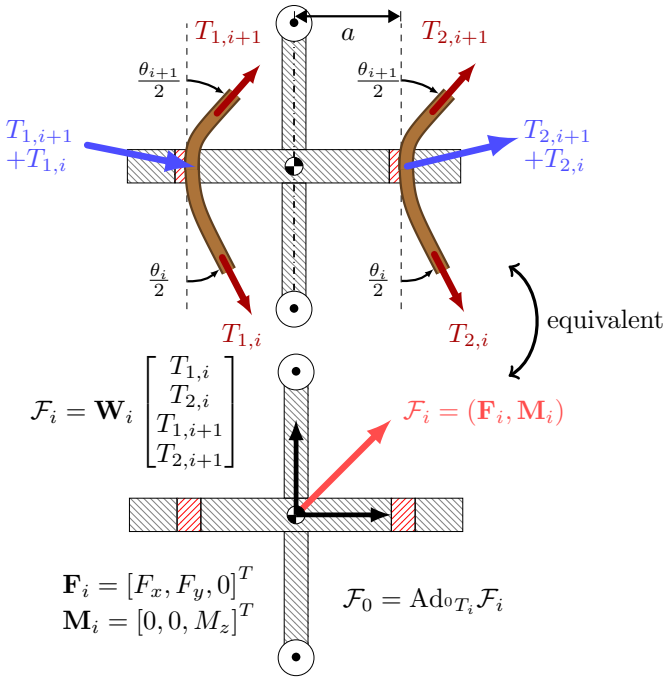

Figure 3. Equivalent body wrenches from cable tensions.

$$\mathbf{J}_S^T = \begin{bmatrix} {}^0\mathbf{J}_0^T & {}^0\mathbf{J}_1^T & {}^0\mathbf{J}_2^T & \cdots & {}^0\mathbf{J}_{n_l}^T \\ & {}^1\mathbf{J}_1^T & {}^1\mathbf{J}_2^T & & {}^1\mathbf{J}_{n_l}^T \\ & & \ddots & \ddots & \vdots \\ & & & \ddots & {}^{n_l-1}\mathbf{J}_{n_l}^T \\ \mathbf{0} & & & & {}^{n_l}\mathbf{J}_{n_l}^T \end{bmatrix} \tag{9}$$

3. SIMULATION AND EXPERIMENTAL SET-UP

3.1 Numerical implementation

Typically, the forward dynamics of tree-like kinematic mechanisms is implemented via specific algorithms and libraries, such as the celebrated recursive Newton-Euler algorithm or the articulated body algorithms; however, to validate the models presented in this work, we have chosen to simulate the equations of motion directly via state space formulation. To this end the authors implemented a small simulation environment for the forward dynamics of a planar Snake-arm section in MATLAB, using analytical expressions obtained for the inertia and Coriolis matrices, as well as the system's jacobian and gravity torque vector. Owing to the presence of dry friction terms in the dynamics, we used MATLAB's *ode15s* solver, which is a variable-size multistep scheme, as recommended by Shampine and Reichelt (1997) for numerically stiff problems.

3.2 The Annelida robot's Snake-arm section

The Annelida robot is an in-pipe inspection robot being developed (at the time of writing) partly by the Laboratory of Mechatronics and Controls (LAMECC) at UFRGS, whose name derives from its' long, slender structure and locomotion method by peristaltic motion. It has a modular structure, where each module is designed with a specific objective in mind. As part of its capabilities, the "Snake-arm" section is being developed in order for the robot

to be able to navigate through tight curves and control its direction of motion when it reaches a tee joint or a manifold. This module can be seen in Figure 4. The Snake-

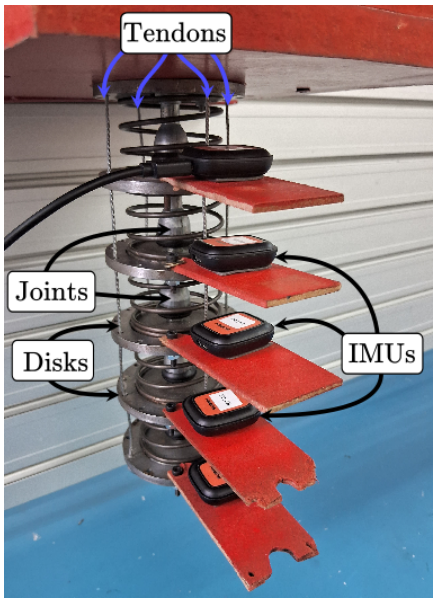

Figure 4. Snake-arm section mounted with the IMUs used in this work.

arm section is composed of five modules, separated by steel discs and joined together via a backbone composed of coil springs and spherical joints. Each module is actuated by a set of four steel cables, fixed at the base and the end tip, distributed equi-radially around the backbone and separated from each other by 90 degrees. The geometric and inertial parameters for each module of this section are given by Table 1, following the nomenclature in Figure 2; the only exception is the final link, which has mass $m = 201.3g$ and second moment of inertia $I = 76822.0g \cdot mm^2$.

Table 1. Snake arm structural parameters

n_j	n_c	a [mm]	b_1 [mm]	b_2 [mm]	m [g]	I [g $\cdot mm^2$]
5	4	32.0	13.5	25.0	222.6	79398.0

3.3 Parameter identification and experimental validation

To validate the modelling approaches, we realized two different tests: the first "static" bending test consisted of slowly pulling on one of the robot's tendons, and fixing it when the tip reached a 90 degree curvature with relation to the base. The second "dynamic" bending test consisted of pulling the robot until it reached the same final angle, then releasing it and measuring the resultant joint angles. On both tests, the robot was placed upside down such that in bending it would be subjected to its' own weight as an external load. Each of the robot's links were equipped with XSens DOT inertial motion units, fixed by small supports on the disks. Ideally, one would use the resulting orientation from all 9 signals (accelerometer, gyroscope and magnetometer) fused via the sensor's (proprietary) embedded extended Kalman filter, however, since the robot's disks are made of a magnetizable alloy, and due to high acceleration forces experienced during the dynamics tests, these readings were deemed as unreliable. As such, we have chosen to infer the joint angles via a simple complementary filter for the "static" test readings, and to use only each sensor's gyroscope readings filtered via a low-pass Butterworth 5th order filter with normalized cutoff frequency of $\frac{1}{6}$ rad/sample in the dynamic tests. The complementary filter merges the estimated joint angles as the weighed sum of the joint angles estimated by the gyroscope and the accelerometer, $\hat{\theta}_g$ and $\hat{\theta}_a$. This is given by the following equation, where α is a controlling parameter, here chosen as $\alpha = 0.9$.

$$\hat{\theta} = \alpha\hat{\theta}_g + (1-\alpha)\hat{\theta}_a \tag{10}$$

The dynamic model presented in (6) contains unknown stiffness terms as well as unknown friction terms, which must be identified in order to validate the dynamic model for simulation. As the actuation system of the Annelida robot was still in development at the time the experiments took place and the model is nonlinear in the parameters, we used a Particle Swarm Optimization (PSO) algorithm, implemented as described in Gomes (2016), to adjust the unknown parameters to the experimental data. For this, we ran 8 different repetitions of the in-plane bending tests (four to the left, four to the right), and adjusted the parameters with 4 of these repetitions, in an interval of 2 seconds for each test.

As an error metric we used the root mean square error of each joint's predicted and measured position and velocities (subscripts p and v), normalized by the standard deviation (NRMSE). The NRMSE of joint i's position for n_t samples is then:

$$NRMSE_{p,i} = \frac{1}{\text{std}\,(\theta_i)}\sqrt{\frac{1}{n_t}\sum_{k}^{n_t}\left(\theta_k - \hat{\theta}_k\right)^2} \tag{11}$$

The objective function to be minimized by the PSO is the NRMSE of the joint velocities, averaged over all n_j joints.

$$\overline{NRMSE}_v = \frac{1}{n_j}\sum_{i}^{n_j} NRMSE_{v,i} \tag{12}$$

4. RESULTS

4.1 Static tests

In order to compare the kinematic and dynamic models of the prototype robot we have chosen to analyze the in-plane bending joint angles resulting from a total angle of curvature of 90 degrees. The resulting comparison can be seen in Figure 5.

In Figure 5a one can see that the joint space angle values as predicted by the rigid body model show good agreement with the values measured from the static tests, whereas the CCK model fails to represent the individual joint angle variation. The corresponding task-space backbone configuration is seen in Figure 5b. The resulting end-tip position is also much closer in this space to that predicted by the rigid body model. This is due to both the tension loss along the cables due to capstan friction, as well as the self-loading owing to the manipulator's low stiffness-to-weight ratio.

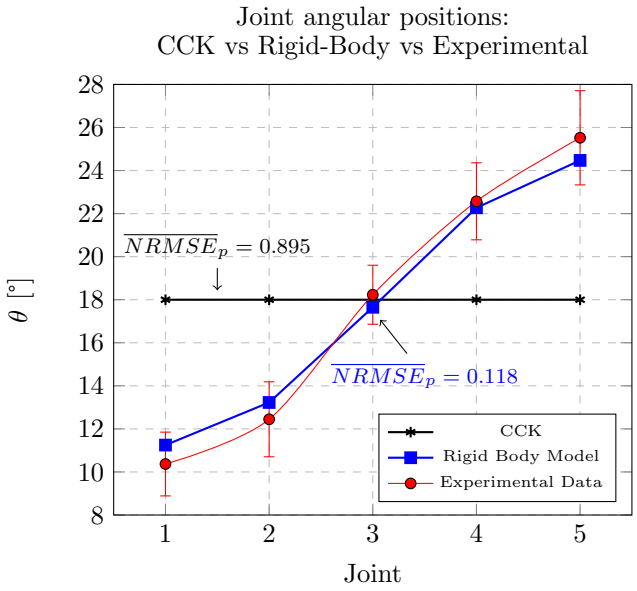

(a) Joint space comparison between measured and predicted joint angles for total bending angle of 90 degrees. The error bars account for the 2.5% and 97.5% quantiles, taken from all eight bending tests.

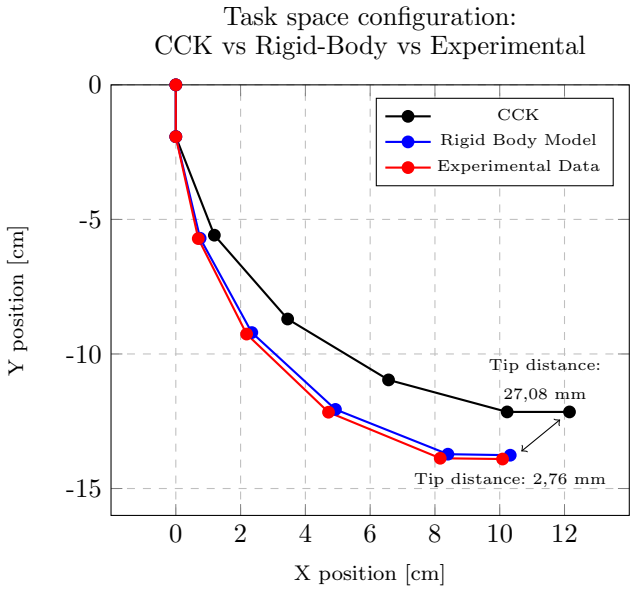

(b) Task space comparison between the sections's backbone as predicted by the CCK model and the dynamic model. The tip distances are the absolute cartesian distance between the section's tip, as measured by the IMUs, and the predicted positions by each model.

Figure 5. Results from the static tests.

4.2 Dynamic tests

The parameters used for the particle swarm parameter fitting procedure are given in Table 2, and the resulting physical values identified for the manipulator section considered in this work are presented in Table 3. To identify the parameters, we used four of the eight repetitions, two bending to the left and two bending to the right. From these, we selected repetitions 1, 2, 5 and 8 for identification, and the rest were used for validation. The resulting NRMSE values are in Table 4, which indicates that the model is able to approximately reproduce the behavior of all of the repetitions using the fitted values.

Table 2. Parameters used in the particle swarm algorithm.

Parameter	Value
# of particles n_p.	20
Max. # of iterations n_{iter}	40
Obj. func. tolerance ε_f	0.001
Coeff. of variation tolerance ε_{cov}	0.0001
Cognitive component λ_1	3
Social component λ_2	2
Velocity momentum ϖ	0.1
Divergence avoiding coefficient χ	0.1146

Table 3. Identified parameter values for the manipulator via PSO algorithm.

Parameter [Unit]	**Value**
K [Nm/rad]	1.2379
τ_μ [N/rad]	0.0314
τ_c [N/rad]	0.0413
S [-]	0.7472
v_d [rad/s]	0.2994

Table 4. Position and velocity $\overline{NRMSE}$ values for each repetition. Repetitions 1, 2, 5 and 8 were used for the parameter identification.

Repetition	$\overline{NRMSE}_p$	$\overline{NRMSE}_v$
1	0.43335	0.68125
2	0.73348	0.65181
3	0.47457	0.62494
4	0.54565	0.60868
5	0.67894	0.58333
6	0.61284	0.64235
7	0.58105	0.63264
8	0.52260	0.67874

Figure 6 compares the estimated joint positions from the IMUs with the angles predicted by the rigid body model. Here the significant friction effects are evident by the steady-state difference between the joint angles and the "straight" configuration ($\theta = 0$). This behavior is successfully modeled by Stribeck friction, and the resulting joint trajectories are similar to those observed experimentally. It is evident from the experiments that the constant curvature approximation does not hold for even this simple case when the robot's stiffness is very low. It is also worth noting that the resultant curvature behavior can be approximated as linearly varying along the joints.

5. CONCLUSIONS

In this paper we present and analyze two common modelling approaches for continuum robotic applications, namely the continuous curvature model and the rigid body model, when applied to a Snake-arm robot section with high dry friction characteristics and a low stiffness-to-weight ratio. Different from other works, in this paper we include both dry joint friction and cable tension loss effects. Both of these models were implemented in MATLAB and the simulation results are compared with the robot section's behavior during in-plane bending, for both static configuration and dynamic behavior. As the robotic section prototype has no joint encoders, we used an indirect measuring method in order to infer the joint angles

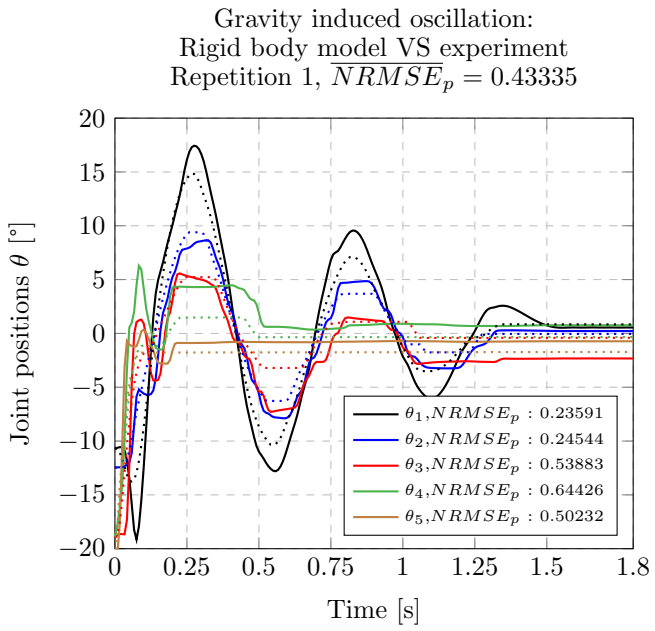

Figure 6. Predicted angular position via rigid body model (solid lines) VS measured (dashed lines) for each joint in repetition 1.

and velocities. For the parameter identification we used a metaheuristic particle swarm optimization algorithm.

The results show that the constant curvature model, although useful for inverse kinematics and as a first approximation for high stiffness continuum robots, falls short of adequately reproducing the actual behavior exhibited by the prototype robot section. In contrast, the traditional rigid body modelling approach was able to reproduce the section's static and dynamic behavior for in-plane loading. As such, we conclude that the constant curvature model, despite its simplicity, is not adequate to represent less-than-ideal continuum robots. One possible improvement for future works is the comparison of the traditional rigid body model with the more refined Cosserat beam models.

ACKNOWLEDGEMENTS

The authors are thankful to Dr. Prof. Renato V. B. Henriques for the IMUs lent for this work. The authors are also thankful for the CAPES scholarship that helped fund this work.

REFERENCES

Allen, T.F., Rupert, L., Duggan, T.R., Hein, G., and Albert, K. (2020). Closed-Form Non-Singular Constant-Curvature Continuum Manipulator Kinematics. In *2020 3rd IEEE International Conference on Soft Robotics (RoboSoft)*, 410–416. doi:10.1109/RoboSoft48309.2020.9116015.

Ay, M. (2023). Modeling and analysis of a modular-structured tendon-driven continuum robot for the three-dimensional end effector coordinate. *Simulation Modelling Practice and Theory*, 127, 102787. doi:10.1016/j.simpat.2023.102787.

Boyer, F., Lebastard, V., Candelier, F., and Renda, F. (2021). Dynamics of Continuum and Soft Robots: A Strain Parameterization Based Approach. *IEEE Transactions on Robotics*, 37(3), 847–863. doi:10.1109/TRO.2020.3036618.

Chirikjian, G. and Burdick, J. (1994). A modal approach to hyper-redundant manipulator kinematics. *IEEE Transactions on Robotics and Automation*, 10(3), 343–354. doi:10.1109/70.294209.

Dupont, P.E., Simaan, N., Choset, H., and Rucker, C. (2022). Continuum Robots for Medical Interventions. *Proceedings of the IEEE. Institute of Electrical and Electronics Engineers*, 110(7), 847–870. doi:10.1109/JPROC.2022.3141338.

Featherstone, R. (2008). *Rigid Body Dynamics Algorithms*. Springer, New York.

Frazelle, C.G. (2021). *Continuum Robots: Interfacing, Modeling, and Automation*. Ph.D. thesis, Clemson University.

Gazzola, M., Dudte, L.H., McCormick, A.G., and Mahadevan, L. (2018). Forward and inverse problems in the mechanics of soft filaments. *Royal Society Open Science*, 5(6), 171628. doi:10.1098/rsos.171628.

Gomes, H.M. (2016). Multi-objective optimization of quarter car passive suspension design in the frequency domain based on PSO. *Engineering Computations*, 33(5), 1422–1434. doi:10.1108/EC-01-2015-0021.

Lynch, K.M. and Park, F.C. (2017). *Modern Robotics: Mechanics, Planning, and Control*. Cambridge University Press, Cambridge, UK.

Mueller, A. (2018). Screw and Lie Group Theory in Multibody Kinematics – Motion Representation and Recursive Kinematics of Tree-Topology Systems. *Multibody System Dynamics*, 43(1), 37–70. doi:10.1007/s11044-017-9582-7.

Murray, R.M., Li, Z., and Sastry, S.S. (1994). *A Mathematical Introduction to Robotic Manipulation*. CRC Press, 1 edition. doi:10.1201/9781315136370.

Renda, F., Boyer, F., Dias, J., and Seneviratne, L. (2018). Discrete Cosserat Approach for Multi-Section Soft Robots Dynamics. *IEEE Transactions on Robotics*, 34(6), 1518–1533. doi:10.1109/TRO.2018.2868815.

Russo, M., Sadati, S.M.H., Dong, X., Mohammad, A., Walker, I.D., Bergeles, C., Xu, K., and Axinte, D.A. (2023). Continuum Robots: An Overview. *Advanced Intelligent Systems*, 5(5), 2200367. doi:10.1002/aisy.202200367.

Shampine, L.F. and Reichelt, M.W. (1997). The MATLAB ODE Suite. *SIAM Journal on Scientific Computing*, 18(1), 1–22. doi:10.1137/S1064827594276424.

Siciliano, B. and Khatib, O. (eds.) (2016). *Springer Handbook of Robotics*. Springer Handbooks. Springer International Publishing, Cham. doi:10.1007/978-3-319-32552-1.

Suh, J.w., Kim, K.y., Jeong, J.w., and Lee, J.j. (2015). Design Considerations for a Hyper-Redundant Pulleyless Rolling Joint With Elastic Fixtures. *IEEE/ASME Transactions on Mechatronics*, 20(6), 2841–2852. doi:10.1109/TMECH.2015.2389228.

Webster, R.J. and Jones, B.A. (2010). Design and Kinematic Modeling of Constant Curvature Continuum Robots: A Review. *The International Journal of Robotics Research*, 29(13), 1661–1683. doi:10.1177/0278364910368147.